Soft Matter

Dynamics of nanoparticle tracers in supercooled nanoparticle matrices

Journal:	*Soft Matter*
Manuscript ID	SM-ART-09-2024-001106.R2
Article Type:	Paper
Date Submitted by the Author:	10-Dec-2024
Complete List of Authors:	Edimeh, Peter; University of Houston Slim, Ali; University of Houston Conrad, Jacinta; University of Houston

Soft Matter

ARTICLE TYPE

Cite this: DOI: 00.0000/xxxxxxxxxx

Dynamics of nanoparticle tracers in supercooled nanoparticle matrices†

Peter Edimeh,[a] Ali H. Slim,[a] and Jacinta C. Conrad*[a]

Received Date
Accepted Date

DOI: 00.0000/xxxxxxxxxx

We investigate the dynamics of tracer nanoparticles in bulk supercooled nanoparticle matrices using confocal microscopy. We mix fluorescent (tracer) and undyed (matrix) charged-stabilized polystyrene nanoparticles with tracer-to-matrix particle size ratios $\delta = 0.34, 0.36, 0.45, 0.71$ at various matrix volume fractions ϕ. Single-particle and collective dynamics were obtained from particle-tracking algorithms and differential dynamic microscopy (DDM), respectively. The long-time behavior of the tracer mean-square displacement (MSD) and the shape of the distributions of particle displacements depend on δ and ϕ. At sufficiently large ϕ, small tracers ($\delta \leq 0.36$) remain mobile and subdiffusive but large tracers ($\delta \geq 0.45$) are dynamically arrested. The relaxation times determined from the intermediate scattering function (ISF) increase with δ and ϕ. Anomalous logarithmic decays in the ISF are observed for tracers of size $\delta \leq 0.36$ over a length scale of four to ten matrix particle diameters. These results provide insight into how penetrant size affects the transport of nanoparticles in porous media with soft interparticle interactions.

1 Introduction

Controlling the dynamics of nanoscale penetrants in heterogeneous media is crucial for advancing industrial and biomedical applications. For instance, nanoparticles can increase oil recovery from reservoirs and thereby improve oil extraction efficiency.[1–7] In medicine, nanoparticles are used as targeted delivery systems to precisely transport theranostic agents to specific sites, offering new capabilities in treatment strategies.[8–13] Incorporating nanoparticles into composite materials significantly enhances their mechanical, optical, and thermal properties.[14] The microenvironments through which nanoparticles navigate through in these applications, including soils, tissues, the extracellular matrix, and polymer solutions and melts, relax on the length and time scales that characterize nanoparticle transport. Thus, understanding how nanoparticles move in dynamic complex media is essential for controlling their spreading.

Model complex media in which dynamics are well characterized provide a useful platform in which to examine the coupling between nanoparticle and environmental dynamics. Media commonly used in such studies include polymer solutions[15–20] and melts;[21–27] emulsions;[28,29] and colloidal gels[30] and supercooled liquids.[31–40] Glass-forming particle liquids are a particularly interesting medium in which to probe nanoparticle transport because the dynamics of supercooled liquids and glasses are spatially and temporally heterogeneous.[41,42] In supercooled liquids, particle dynamics are arrested on intermediate time scales but relax on long time scales. Arrest on intermediate time scales is due to the formation of cages of particles,[43,44] which must relax to recover diffusive dynamics on long time scales. Thus, relaxations in these supercooled liquids occur cooperatively[45]. The size of cooperatively relaxing regions increases with the particle volume fraction ϕ[46,47], and the shape depends on the interactions between the matrix particles[48]. Suspensions at sufficiently high ϕ form glasses whose dynamics are arrested on experimentally accessible time scales.[47,49,50] Thus, particle supercooled liquids and glasses are often used as model media in which to examine how penetrant motions couple to collective dynamics in slowly-relaxing matrices.

Tracer particles in glassy particle liquids couple to different matrix dynamics depending on the relative size of the tracer and matrix particles δ.[34,36,39,51] The motion of tracer particles with $\delta > 0.35$ approximately couples to the matrix relaxations, whereas tracers with $\delta < 0.35$ diffuse within the void space of the matrix.[34,36,38] Intriguingly, tracers of size $\delta = 0.35$ exhibit anomalous transport, signaled by logarithmic relaxations of the intermediate scattering function,[34,36], indicating that their motion couples both to matrix relaxations and local fluctuations. These stud-

[a] William A. Brookshire Department of Chemical and Biomolecular Engineering, University of Houston, 4226 Martin Luther King Boulevard, Houston, Texas 77204-4004, USA. Fax: +1 713-743-4323; Tel: +1 713 743 3829; E-mail: jcconrad@uh.edu

† Supplementary Information available: Procedure for matrix volume fraction measurement; particle tracking resolution limits summarized in Table S1 and supplementary tracking figures; theoretical minimum $q_{\min}$ summarized in Table S2 and supplementary collective dynamics figures; comparison of q-dependent single-particle dynamics ($f^{\text{self}}(q,\tau)$ from SPT) with collective dynamics ($f(q,\tau)$ from $D(q,\Delta\tau)$); hard-sphere mapping. See DOI: 10.1039/cXsm00000x/

ies, however, have largely been carried out using micron-sized colloids (i.e., where tracers and matrix particles are at least 500 nm in size) and the length scale of interparticle interactions (particularly, electrostatics) is small compared to the particle diameter. In many media of practical interest, however, characteristic length scales of the medium and penetrants are of order 100 nm, motivating studies of dynamic coupling in nanoparticle suspensions.[52,53].

In this study, we examine the coupling between the dynamics of tracer nanoparticles and those of bulk supercooled nanoparticle matrices. We formulate binary mixtures of large (140 nm) and small (120 nm) charge-stabilized polystyrene (PS) nanoparticles at an 80:20 ratio to frustrate crystallization,[54] and add charge-stabilized PS tracer nanoparticles to obtain various tracer-matrix size ratios ($\delta = 0.34, 0.36, 0.45, 0.71$). We image the tracers over time in matrices of various volume fraction ϕ using confocal microscopy and analyze the images using single-particle tracking and differential dynamic microscopy. Single-particle tracking analyses reveal that tracer dynamics in nanoparticle glasses depend on δ, coupling to arrested matrix dynamics for the largest $\delta = 0.71$ tracers at large ϕ. Small tracers, however, are able to escape local cages and relax on long time scales, suggesting that these particles couple to different dynamical processes within the matrix. Differential dynamic microscopy analyses reveal that tracers of size $\delta \approx 0.35$ exhibit the anomalous logarithmic relaxations in the intermediate scattering function previously observed for larger colloidal particles, suggesting that their dynamics couple both to matrix fluctuations and relaxations, but on somewhat longer length scales of four to ten matrix particle diameters.

2 Materials and Methods

2.1 Preparation of supercooled nanoparticle matrices

Aqueous suspensions of undyed charge-stabilized polystyrene (PS) nanoparticles with diameters $\sigma_{\mathrm{matrix(i)}} = 140$ nm and $\sigma_{\mathrm{matrix(ii)}} = 120$ nm (both with dispersity of ~ 0.08 and initial volume fraction $\phi = 0.1$) were acquired from Thermo Fisher Scientific and used as matrix particles. Fluorescently labeled and charge-stabilized PS nanoparticles with diameter $\sigma_s = 47$ nm (green) and 51, 63, and 100 nm (red) were also purchased from Thermo Fisher Scientific and used as tracer particles (Fig. 1(a)); we define $\delta = \sigma_s/\sigma_{\mathrm{matrix(i)}}$. The zeta potentials ζ of the nanoparticles were determined using a Nicomp 380 ZLS zeta sizer. The zeta potentials of the PS particles in deionized water (Millipore, 18.2 MΩ-cm) ranged from -45 to -15 mV (Fig. 1(b)).

The fluorescent tracer particles were dispersed in deionized water at dilute volume fractions between 6.5×10^{-7} and 2×10^{-5} to mitigate aggregation and minimize their influence on the bulk structure, thermodynamics, and dynamics of the matrix. To generate the bulk supercooled matrix, the undyed PS particles were mixed at the Kob-Anderson volume ratio of $\sigma_{\mathrm{matrix(i)}}$: $\sigma_{\mathrm{matrix(ii)}}$ = 80:20 to prevent crystallization.[54] Approximately 1 μL of the dilute fluorescent tracer particle suspension was added to 400 μL of the matrix suspension. Subsequently, the suspensions were centrifuged at 8000 rpm for a given duration to obtain a specified final PS ϕ. Details of the determination of the PS volume fraction are provided in the ESI.

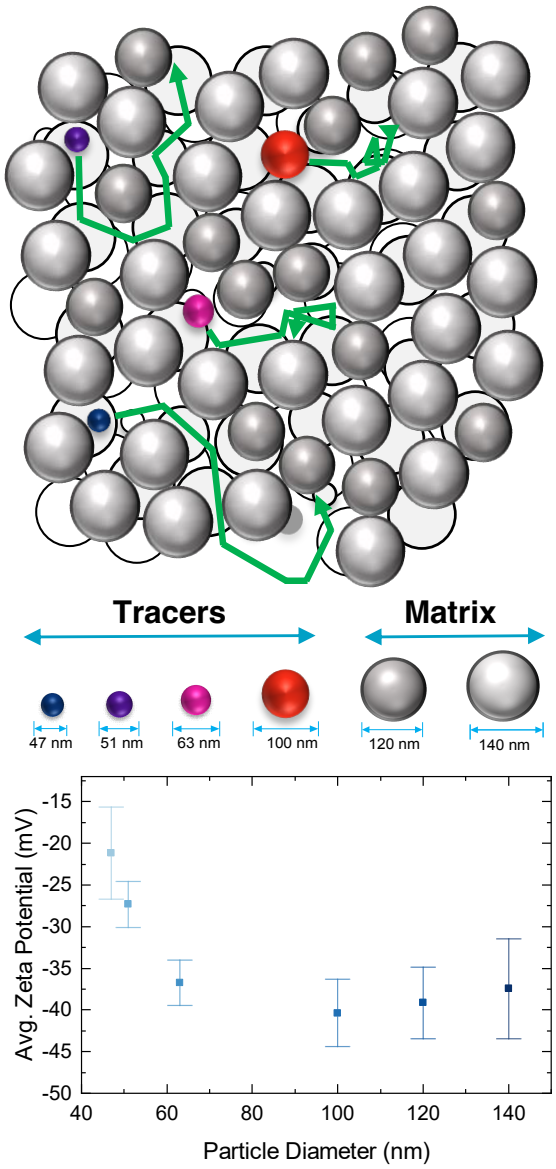

Fig. 1 (a) Schematic representation of tracers of various sizes in a 3-D supercooled matrix. The relative sizes of (left) tracer and (right) matrix particles used in this study are depicted under the schematic. (b) Zeta potential ζ as a function of particle diameter σ. The error bars indicate the standard deviation of the measurements.

2.2 Preparation of bulk supercooled liquid samples

Custom sample chambers were constructed by drilling 4.8 mm diameter wells into standard microscope slides (VWR, 75 mm × 25 mm × 1 mm). The cut glass slides (37 mm × 25 mm × 1 mm) were cleaned with isopropyl alcohol, air-dried, and attached onto a larger cover slide (Gold Seal, 48 mm × 65 mm × 0.15 mm) using UV-curable epoxy (Norland Optical Adhesive 81). This assembly formed a chamber with depth of approximately 0.8 mm, which is ~5700 times the average matrix particle size. Immediately after centrifugation, the supercooled nanoparticle suspensions were placed in this well, covered with a coverslip (Fisher-

brand, 22 mm × 22 mm), sealed with UV-curable epoxy, and used in imaging experiments.

2.3 Confocal imaging and particle tracking analysis

Tracer particles in supercooled matrices were imaged using a Leica DMi8 inverted fluorescence microscope equipped with a Leica SP8 confocal head and a 100x oil immersion objective (NA = 1.40). For each suspension, multiple time series of 2-D images, consisting of 8000 frames acquired at a frame rate of 50 frames per second (fps), were captured at a vertical position of 30 μm above the bottom of the coverslip to access bulk dynamics away from the chamber walls. For each sample, four to five time series were acquired at different positions within the sample to ensure statistically robust and reliable data analysis. In each frame, the typical number of tracked particles ranged between 15 and 30. The pixel size in the captured images ranged from 0.076 to 0.228 μm per pixel, which was larger than the tracer particle size in each system (Table S1). Images using a pixel size of 0.076 μm were were 256 pixels × 256 pixels (19.5 μm × 19.5 μm); images using a pixel size of 0.228 μm were 256 pixels × 256 pixels (58.4 μm × 58.4 μm). (A complete list of imaging conditions is provided in Table S1.)

We employed single-particle tracking algorithms[55] to locate the tracer particle centroids in each image and link them into trajectories. The experimental suspensions are 3-D bulk systems; because the dynamics of tracer nanoparticles are very fast, however, we track the tracers in 2-D. The 2-D tracking resolution ε was calculated as the square root of the y-intercept of a linear fit of tracer MSD in a glycerol/water mixture (to mimic the higher viscosity of the nanoparticle solutions) and were determined for each (δ,ϕ) combination based on the pixel size used in a given experiment (Table S1) and are shown on the figures for mean-square displacements and distributions of particle displacements.

From the trajectories, we calculated the 2-D ensemble-averaged mean-square displacement $\mathrm{MSD}(\tau)=\langle\Delta r^2(\tau)\rangle=\langle[x(t+\tau)-x(t)]^2\rangle+\langle[y(t+\tau)-y(t)]^2\rangle$, where τ is the lag time, $x(t)$ and $y(t)$ are the x and y positions of the tracer particle at time t, and $\langle...\rangle$ denotes an ensemble average. We also calculated the self part of the van Hove correlation function $\mathrm{G_s}(x,t)=\frac{1}{N}\sum_{i=1}^{N}\langle\delta\left(x-[x_i(t)-x_i(0)]\right)\rangle$, where N is the number of particles in the system and $\delta(x)$ is the Dirac delta function. Finally, to assess the extent to which the distribution of particle displacements deviated from the Gaussian statistics expected for Fickian diffusion, we calculated the 2-D non-Gaussian parameter $\alpha_2(\tau)=3\langle\Delta r^4\rangle/5\langle\Delta r^2\rangle^2-1$, where $\langle\Delta r^2\rangle$ and $\langle\Delta r^4\rangle$ are the second and fourth moments of the displacement distribution. The -1 ensures that $\alpha_2=0$ for a Gaussian distribution.

2.4 Differential dynamic microscopy

To characterize the collective tracer dynamics within our samples, we employed Differential Dynamic Microscopy (DDM) to examine the temporal evolution of spatial correlations in the sample.[56] In the DDM method, the intensity difference $\Delta I(x,y,\tau)=I(x,y,t_0+\tau)-I(x,y,t_0)$, where $I(x,y,t_0)$ is the intensity of a 2D image at time t_0, is calculated for each delay time τ. The squared magnitude of the Fourier transform of $\Delta I(x,y,\tau)$ is computed and averaged over all starting times t_0 to obtain the image structure function $D(q,\tau)=\langle|\widetilde{\Delta I}(q,\tau)|^2\rangle_t$, where q is the 2D wavevector in Fourier space and $\langle...\rangle_t$ denotes a time average. The intermediate scattering function (ISF) $f(q,\tau)$ is obtained from the image structure function via $D(q,\tau)=A(q)[1-f(q,\tau)]+B(q)$. In this equation $A(q)$ is the static amplitude, which depends on the details of the imaging system and the sample structure, and $B(q)$ represents the background noise. The background B is estimated by the minimum of the DDM matrix, $B(q)\cong B=\min[D(q,\tau_{\min})]$[57,58], since the value of B is approximately constant for the range of wavevectors accessible in this study. Using B, we estimate $A(q)=2\times\langle|\widetilde{I}(q,t)|^2\rangle_t-B$. Subsequently, we calculate $f(q,\tau)=1-[D(q,\tau)-B]/A(q)$. The decay of $f(q,\tau)$ over time describes the decorrelation in particle density fluctuations over the length scale $2\pi q^{-1}$. For this study, we used a Python-based implementation of DDM, PyDDM.[58]

The range of wavevectors accessible in DDM is determined by the experimental geometry.[59] The minimum wavevector $q_{\min}=\frac{2\pi}{N\Delta_x}$, where $N=256$ is the number of pixels along one dimension of an image, and Δ_x is the pixel size.[59] The maximum wavevector $q_{\max}=2\pi\mathrm{NA}/\lambda=15.849\ \mu\mathrm{m}^{-1}$, where $\lambda=550$ nm is the wavelength of incident light. The theoretical $q_{\max}$ is constant for all samples because λ and NA were not varied between experiments. In practice, however, these theoretical limits were not accessible in these experiments due to the time scale of the tracer dynamics and the limitations of the frame rate and number of frames.[60] At high q, the camera's frame rate was insufficient to capture the fast dynamics of small tracers. Hence, we restricted $q_{\min}$ to 0.65 and 1.29 $\mu\mathrm{m}^{-1}$ for large ($\delta=0.71$) and small ($\delta=0.34$) tracers, respectively, yielding values of the normalized wavevector $q\sigma_s=0.065$ and 0.061, respectively (Table S2 in the ESI). These values correspond to wavevectors where the ISF exhibits a decay. Similarly, we selected as $q_{\max}$ the wavevector at which the ISF begins to decrease to ensure reliable data. The selected $q_{\min}$ and $q_{\max}$ values give the range of $q\sigma_s$ values, all of which fall within the theoretical expectations.

3 Results and Discussion

3.1 Single-particle dynamics

We imaged PS tracer nanoparticles of four relative sizes ($\delta=0.34,0.36,0.45,0.71$) in supercooled PS nanoparticle matrices using confocal microscopy. Temporal color maps showing the position of the tracer particles over time clearly depict that the spreading of tracers in the matrices depends on δ (Fig. 2). The trajectories of tracers with $\delta=0.34$ and 0.36 reveal that these particles are able to move further distances than the larger ($\delta=0.45,0.71$) tracers over the same time interval. Further, the tracers undergo a transition from delocalized ($\delta=0.34$) to localized ($\delta=0.71$) on the time scales of our experiments.

We characterize the dynamics of individual particles by calculating the mean-square displacements (MSDs) for tracers in matrices of various volume fractions ϕ. To compare dynamics across tracer sizes and matrix volume fractions, we normalize the MSD by the square of the tracer diameter σ_s^2 and the time

Fig. 2 Temporal color map of the positions of tracer nanoparticles after 160 seconds (8000 frames) for (a) $(\delta,\phi) = (0.34, 0.49)$, (b) $(\delta,\phi) = (0.36, 0.48)$, (c) $(\delta,\phi) = (0.45, 0.49)$ and (d) $(\delta,\phi) = (0.71, 0.49)$ showing δ-dependent relaxations.

by the time scale for Brownian diffusion of the tracer particle $\tau_0 = 3\pi\eta\sigma_s^3/k_BT$. For the largest tracer particle ($\delta = 0.71$), the tracer MSDs exhibit a plateau on short time scales due to transient caging by the matrix particles (Fig. 3(a)). For $\phi \leq 0.47$, the matrix is able to relax on long time scales, allowing the tracer to escape this transient cage. For tracers in these matrices, the tracer MSDs increase as a power law with time on long time scales such that MSD $\sim \tau^\alpha$ with $\alpha < 1$. The exponent α decreases with increasing ϕ, indicating that the tracer dynamics are increasingly subdiffusive as caging increases. For $\phi = 0.49$, however, the tracer dynamics are arrested on all time scales and fall below the tracking resolution indicated by the dashed line in Fig. 3(a). Further, experiments extending two orders of magnitude further in time still show arrested dynamics that fall below the resolution limit (Fig. S2). The tracer dynamics are significantly faster for a given matrix ϕ when δ is decreased from 0.71 to 0.34 (Fig. 3(b)). Furthermore, the dynamics of the small tracers are subdiffusive on long time scales even at the highest $\phi = 0.52$ studied. Together, these observations suggest that smaller tracers are less confined and thus move more easily through the matrix voids than larger tracers.[61,62]

Comparison of the MSDs for various δ in a $\phi = 0.49$ matrix reveals a transition from subdiffusive to arrested dynamics upon increasing δ (Fig. 3(c)). Large tracers ($\delta = 0.71$) are strongly caged on all accessible time scales, whereas smaller tracers ($\delta = 0.45$ and $\delta = 0.34$) are able to escape their cages on long time scales. The height of the intermediate plateau decreases with increasing δ, consistent with previous studies,[34,36–38] showing that larger tracers are more strongly confined. Further, the change from strongly localized to subdiffusive dynamics with decreasing δ is also consistent with an earlier study of micron-sized particles that showed that penetrants whose relative size exceeded a critical value $\delta_c \approx 0.35$ exhibited glassy intruder dynamics, characterized by strong localization and a plateau in the MSD.[34]

To examine how the tracer mobility varies with ϕ, we compare the normalized MSD $\langle \Delta r^2/\sigma_s^2 \rangle$ for tracers of various sizes at two time points. For a short normalized lag time ($\tau/\tau_0 = 4 \times 10^2$), $\langle \Delta r^2/\sigma_s^2 \rangle$ decreases by approximately one order of magnitude as ϕ is increased from 0.45 to 0.52 (Fig. 4(a)), indicating that ϕ does not markedly affect the short-time displacement. On a longer normalized lag time ($\tau/\tau_0 = 4.5 \times 10^4$), the normalized MSD decreases by approximately 2.5 orders of magnitude as the matrix volume fraction is increased from $\phi = 0.45$ to 0.52 (Fig. 4(b)). For the four tracer sizes examined in this study, the MSDs of the

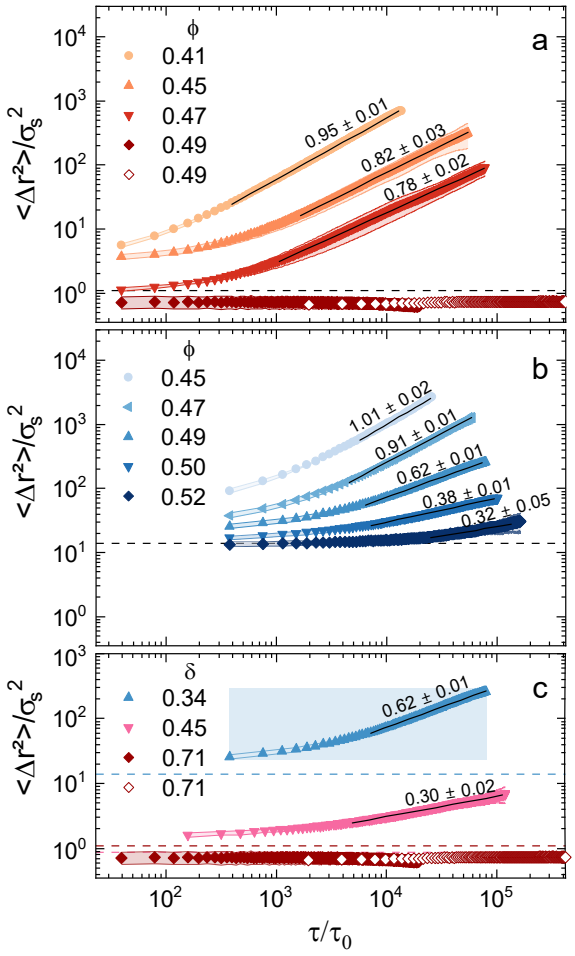

Fig. 3 Tracer dynamics from single particle tracking. (a, b) Ensemble averaged mean-squared displacement (MSD) $\langle \Delta r^2 \rangle$ normalized by tracer diameter σ_s^2 as a function of lag time τ normalized by Brownian diffusion time τ_0 for various ϕ at size ratios δ of (a) 0.71 and (b) 0.34. (c) MSD at constant $\phi = 0.49$ for various δ. The open diamond symbols represent data from a longer duration experiment. Solid black lines indicate the scaling exponent α, obtained from the slope of a linear fit to the MSD versus τ/τ_0 data on long times, where MSD $\propto \tau^\alpha$. The MSD is diffusive when $\alpha = 1$ and subdiffusive when $\alpha < 1$. The dashed lines represent the normalized tracking resolution ε. Error bars indicate one standard deviation over at least four replicates per state point.

smaller tracers near the critical $\delta_c = 0.35$ of Ref. 34 are consistently one order of magnitude larger than those of larger tracers ($\delta = 0.45, 0.71$) on short time scales and between 1 – 2 orders of magnitude larger than those of the larger tracers on long time scales (with the deviation increasing with ϕ). This result is consistent with previous studies showing that the nature of the tracer motion changes near δ_c.[34,36,37]

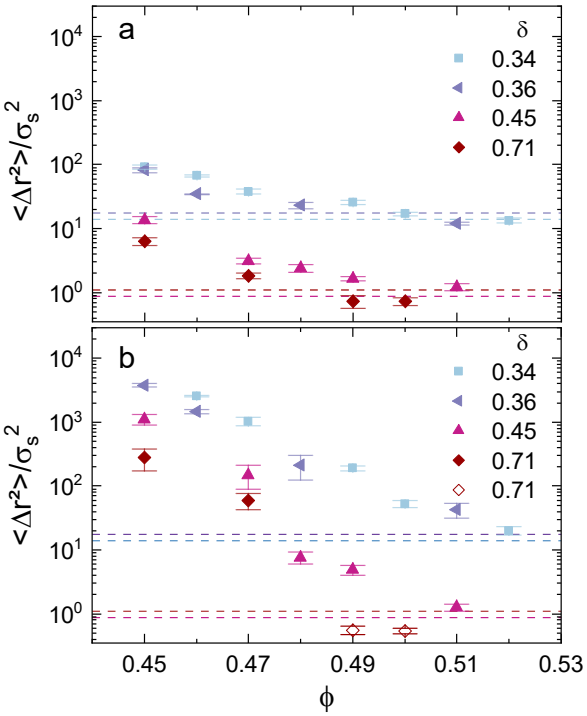

Fig. 4 Summary of tracer dynamics from MSDs. $\langle \Delta r^2/\sigma_s^2 \rangle$ as a function of ϕ at (a) $\tau/\tau_0 = 4 \times 10^2$ and (b) $\tau/\tau_0 = 4.5 \times 10^4$. The open diamond symbols represent data from a longer duration experiment. The colored dashed lines represent the normalized tracking resolution ε for each δ. The error bars indicate one standard deviation over at least four replicates per state point.

The displacement distributions for large tracers ($\delta = 0.71$) progressively narrow with increasing matrix ϕ due to greater confinement. The displacement distribution is Gaussian for $\phi = 0.45$, even though the MSD is slightly subdiffusive on this time scale (see Fig. 3(a)) and non-Gaussian for $\phi \geq 0.47$ (Fig. 5(a)). The displacement distributions for $\delta = 0.34$ also narrow with increasing ϕ and are non-Gaussian at the ϕ examined in our experiments (Fig. 5(b)). At comparable ϕ, the normalized displacements for $\delta = 0.34$ tracers are larger than those for the large $\delta = 0.71$ tracers.

Non-Gaussian displacements of particles in supercooled and glassy matrices are typically attributed to dynamical heterogeneity.[50] To clarify the origins of non-Gaussian displacement distributions for tracer particles of various sizes, we examine the time dependence of the non-Gaussian parameter α_2, which quantifies the degree to which tracer displacements deviate from a Gaussian distribution. For $\delta = 0.71$, α_2 is approximately independent of time and does not change significantly as ϕ increases from 0.41 to 0.49 (Fig. 6(a)). We note that the displacements in the

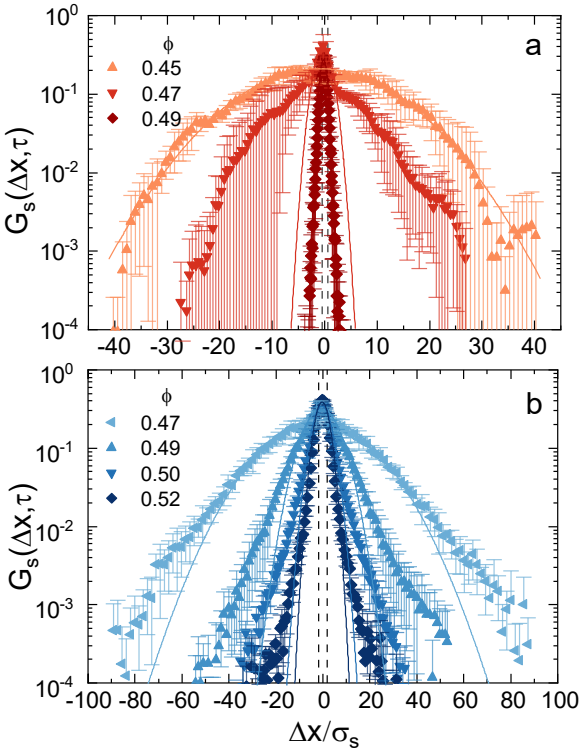

Fig. 5 Normalized probability distribution of tracer displacements $G_s(\Delta x, \Delta\tau)$ as a function of normalized displacement $\Delta x/\sigma_s$ at $\tau/\tau_0 = 4.5 \times 10^4$ s for tracers with δ of (a) 0.71 and (b) 0.34 in matrices of various ϕ. The solid lines are fits to a Gaussian distribution. The black dashed line represents the tracking resolution ε. The error bars indicate one standard deviation over at least four replicates per state point.

$(\delta, \phi) = (0.71, 0.49)$ sample are below the minimum resolution of the tracking algorithm, and so our ability to quantify the distribution shape is limited for this sample. By contrast, for a smaller tracer with $\delta = 0.34$ we find that α_2 evolves with both time and ϕ (Fig. 6(b)). The sample with $(\delta, \phi) = (0.34, 0.49)$ exhibits a weak local maximum near $\tau/\tau_0 \approx 7 \times 10^3$. The position of this weak maximum shifts to longer lag times, $\tau/\tau_0 \approx 3 \times 10^4$, for the $(\delta, \phi) = (0.34, 0.50)$ sample. At the highest $\phi = 0.52$ examined, α_2 sharply increases with time for the experimentally accessible time scales and we are not able to resolve the position of the maximum. The time and ϕ evolution of α_2 for samples with $\delta = 0.36$ is qualitatively similar to those of the $\delta = 0.34$ samples (Fig. S3(b)). Samples with $\delta = 0.45$, however, exhibit local maxima in α_2 for $\phi = 0.47$ and $\phi = 0.48$ within the experimentally accessible time scales; for $\phi \geq 0.50$, however, α_2 is again approximately time-independent (Fig. S3(a)).

The results presented in Fig. 6 suggest that differences in the non-Gaussian parameter arise in part because tracers of different sizes have different propensities to escape the cages formed by the matrix particles. We therefore expect that the ability of the matrix particles to localize the tracers will depend on δ and ϕ. As a metric for localization, we determined the smallest displacement Δx_c at which the displacement distribution for a given (δ, ϕ) deviates from a Gaussian distribution (that is, where the difference exceeds 10%, Fig. 7(a) inset).[63] This metric provides

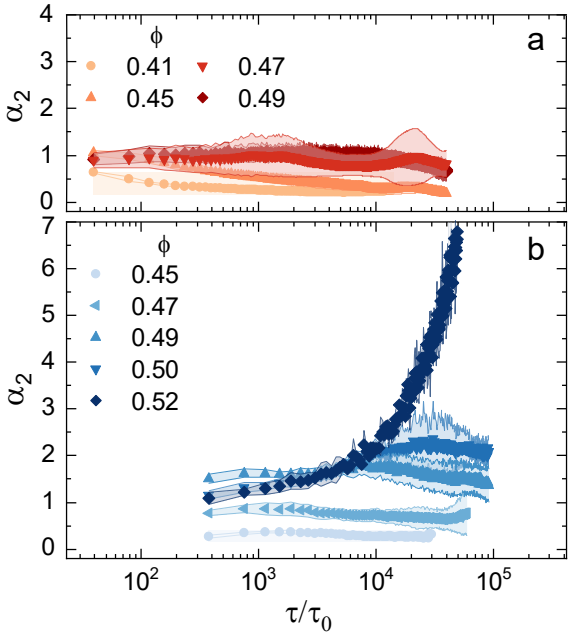

Fig. 6 2-D Non-Gaussian parameter α_2 as a function of normalized lag time τ/τ_0, where τ_0 is the Brownian diffusion time for each tracer, at various ϕ at size ratios δ of (a) 0.71 and (b) 0.34. The error bars indicate one standard deviation over at least four replicates per state point.

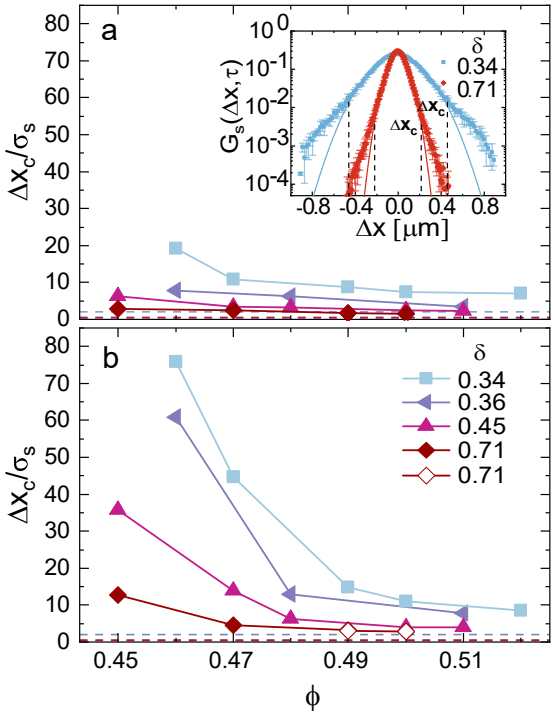

Fig. 7 Normalized length scale at which the distribution of displacements deviates from a Gaussian distribution $\Delta x_c/\sigma_s$ as a function of matrix volume fraction ϕ for various δ at τ of (a) 0.02 s and (b) 1.00 s. The open diamond symbols represent data from a longer duration experiment. The inset to (a) shows Δx_c at $\phi = 0.47$ for $\delta = 0.71$ and $\delta = 0.34$ at $\tau = 0.02$s. The displacement distributions for ($\delta = 0.71$, $\phi = 0.41$), ($\delta = 0.36$, $\phi = 0.45$), and ($\delta = 0.34$, $\phi = 0.45$) were Gaussian. The colored dashed lines represent the normalized tracking resolution ε for each δ. The error bars indicate one standard deviation over at least four replicates per state point.

an estimate of the length scale over which tracers are able to diffuse freely in their local environments on a given time scale. For constant δ, Δx_c decreases with ϕ on both short (0.02 s, Fig. 7(a)) and long (1 s, Fig. 7(b)) time scales. This decrease is more pronounced on long time scales, because small tracers at relatively low ϕ are able to escape cages and diffuse more readily (c.f. Fig. 3). For a given $\phi \lesssim 0.5$, Δx_c decreases as δ is increased. This result indicates that larger particles exhibit non-Gaussian dynamics on smaller length scales, in accord with their coupling to the caged matrix dynamics. Once the matrix is arrested, however, the tracer size no longer strongly affects Δx_c.[38] We note that Δx_c at high ϕ is slightly larger for the small tracers ($\delta = 0.34, 0.36$) than the large tracers ($\delta = 0.45, 0.71$), indicating that the small tracers are slightly less localized even when the matrix is arrested. This result is consistent with earlier studies showing that tracers of size $\delta \approx 0.35$ are able to couple both to matrix fluctuations as well as relaxations,[34,38] which allows them to escape even from arrested cages.

Together, the single-particle tracking results presented in Figures 3 through 7 and S1 through S3 show that the coupling of tracer dynamics and matrix dynamics depends strongly on the relative tracer size δ. The dynamics of small tracers ($\delta \leq 0.36$) are subdiffusive on long time scales even up to the greatest accessible ϕ. Their MSDs relative to tracer size decrease modestly and α_2 increases as ϕ is increased. Large tracers of size $\delta = 0.71$, by contrast, become trapped in cages of matrix particles at higher ϕ. Their dynamics (i.e., $\langle \Delta r^2/\sigma_s^2 \rangle$) decrease markedly as ϕ is increased, but because they remain trapped in cages on long time scales the distributions of displacements are only modestly non-Gaussian (i.e., α_2 remains low). These findings are consistent with experiments[34] and simulations[36,38] that show pronounced differences in tracer dynamics as a function of tracer size and matrix ϕ emerging near $\delta \approx 0.35$; tracers of this size are able to couple both to matrix relaxations and fluctuations.

3.2 DDM measurements of collective dynamics

To examine how tracer dynamics couple to matrix relaxations on larger length scales, we also analyze the microscopy movies using differential dynamic microscopy (DDM). Representative DDM image structure functions $D(q,\tau)$ are shown in Fig. S4, S5 and S6.

For large tracers ($\delta = 0.71$, 0.45) the ISF determined from the DDM analysis as described in §2.4 decays exponentially for a matrix with $\phi = 0.45$, consistent with normal diffusion (Fig. 8(a), S7(a)). At $\phi = 0.49$, however, the ISFs do not decay to zero on experimentally accessible time scales for any q (Fig. 8(b), S7(b)), consistent with the near arrest observed in the single-particle MSDs. The decay of the ISFs for small tracers ($\delta = 0.34$, 0.36) at a relatively low matrix fraction ($\phi = 0.45$) are also exponential, although the fast dynamics of tracers limit the accessible range of wave vectors (Fig. 8(c), S7(c)). Increasing the matrix fraction to $\phi = 0.49$ and $\phi = 0.48$ respectively leads to slower tracer dynamics that still decorrelate over the accessible range of wavevectors (Fig. 8(d), S7(d)). Again, this observation is consistent with the

long-time relaxation observed in the single-particle MSDs.

We calculated the self-intermediate scattering function ($f^{\mathrm{self}}(q,\tau)$), which isolates the motion of individual particles and thus provides insight into local dynamics and relaxation processes independent of collective behavior or correlated motion between particles, from tracer trajectories. Specifically, $f^{\mathrm{self}}(q,\tau) = \frac{1}{N}\sum_{m=1}^{N}\left\langle e^{-j\mathbf{q}\cdot[\mathbf{r}_m(t_0+\tau)-\mathbf{r}_m(t_0)]}\right\rangle_{|\mathbf{q}|=q,t_0}$ [64]. The $f^{\mathrm{self}}(q,\tau)$ and the collective ISF determined from the DDM analysis are in near-quantitative agreement (Fig. S9), particularly at lower volume fractions ($\phi \leq 0.47$) where particle displacements are approximately Gaussian.[65] We also note that because DDM does not require tracking particles, it is able to access slightly longer lag times than SPT.

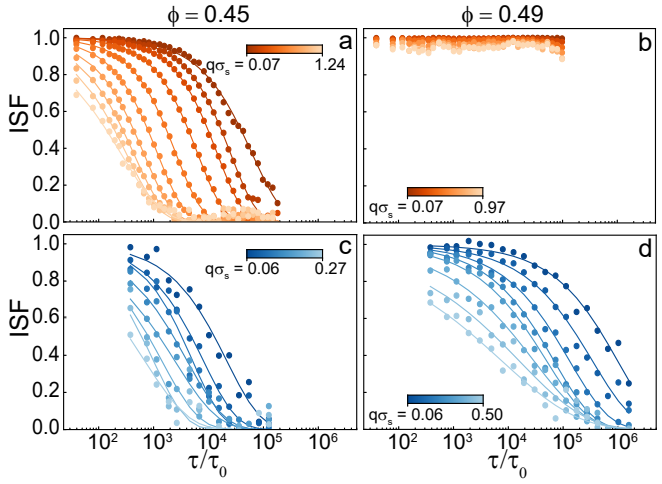

Fig. 8 Tracer dynamics from differential dynamic microscopy (DDM). Collective intermediate scattering function $f(q,\tau)$ as a function of normalized lag τ/τ_0 exhibits a stretched exponential decay for (δ, ϕ) = (a) (0.71, 0.45), (b) (0.71, 0.49), (c) (0.34, 0.45), and (d) (0.34, 0.49). The lines in (a), (c), and (d) indicate fits of the data to a stretched exponential function. Fitting parameters are shown in Table S3.

We compare the collective dynamics across the range of accessible ϕ by examining the behavior of the intermediate scattering function $f(q,\tau)$ of tracers at $q\sigma_s \approx 0.07$, which is close to the largest accessible length scale for tracer size σ_s. To compare across tracer sizes, the lag time is normalized by the $q-$dependent relaxation time $\tau_0(q\sigma_s) = \tau_0 q^2\sigma_s^2$ for $q\sigma_s \approx 0.07$. For the largest tracer ($\delta = 0.71$), $f(q,\tau)$ decays to zero for $\phi \leq 0.47$ but remains arrested on experimentally accessible time scales for $\phi = 0.49$ (Fig. 9(a)). By contrast, the motions of small tracers ($\delta = 0.34$) are able to decorrelate on experimentally-accessible time scales even up to matrix volume fractions of $\phi = 0.50$.

For certain samples with $\delta = 0.34$ and 0.36, we observe an anomalous logarithmic decay of $f(q,\tau)$ that persists for at least two decades in time (Fig. S10 and Table S6). Such decays, however, do not appear for samples with larger δ in the range of ϕ for which we observe relaxations in these experiments. The size ratio $\delta \approx 0.35$ required for anomalous dynamics is consistent with the value ($\delta_c = 0.35$) identified in earlier experiments and simulations.[34,36,37] The length scales over which we observe these anomalous dynamics at $\delta \approx 0.35$, however, are larger than those determined for micron-sized colloids. In Ref. 34 anomalous dynamics in micron-sized colloids occurred at $q^*\sigma_{\mathrm{matrix}} \approx 3.5$, corresponding to a length scale $L^* \approx 1.8\sigma_{\mathrm{matrix}}$. In our experiments, the longest duration of logarithmic decay of $f(q,\tau)$ ($\sim$ 2.5 decades) occurs for $(\delta,\phi) = (0.34, 0.49)$ at $q^*\sigma_{\mathrm{matrix(i)}} \approx 1.09$, corresponding to a length scale $L^* \sim 2\pi\sigma_{\mathrm{matrix(i)}}/1.09 \approx 0.807\ \mu\mathrm{m} \approx 5.8\sigma_{\mathrm{matrix(i)}}$. For other samples, the $q^*\sigma_{\mathrm{matrix(i)}}$ values for which $f(q,\tau)$ exhibits a logarithmic decay correspond to L^* of 4 to $10\times\sigma_{\mathrm{matrix(i)}}$ (Table S6).

We speculate that this difference in length scale may arise from differences in the nature of the matrix interactions (nearly-hard-sphere in Ref. 34, electrostatically repelling in this study). We note, however, that in our previous study of silica nanoparticle tracers in a PS nanoparticle matrix[37] the critical size ratio δ_c was calculated using the effective size of the silica tracers accounting for the electrostatic repulsion using the Barker-Henderson formalism.[66,67] The effective size ratios δ_{eff} for the tracer particles in this study determined using the Barker-Henderson formalism are shown in Tables S4 and S5. Depending on the ionic strength of the solvent, δ_{eff} for the smallest tracers (nominal $\delta = 0.34$) is 0.34 (assuming a Debye length $\kappa^{-1} = 1$ nm) or 0.40 (assuming $\kappa^{-1} = 10$ nm). This comparison suggests that the differences between the nominal and effective δ are not pronounced in this study, in contrast to the large change in effective size that we obtained when the tracer and matrix particles were chemically dissimilar.[37]

We note, further, that $q^*\sigma_{\mathrm{matrix(i)}}$ increases with ϕ at constant δ. For $\delta = 0.34$, these ϕ span the apparent arrest transition in the matrix, which occurs in the range $0.47 \leq \phi \leq 0.49$ (c.f. Fig. 3(a), assuming that the large $\delta = 0.71$ tracers approximately couple to matrix relaxations). Thus, $L^*(\phi)$ for $\delta = 0.34$ decreases across this arrest transition. This result is in contrast to the size of relaxing (mobile) regions in colloidal supercooled liquids and glasses on ϕ, which exhibits a maximum near the glass transition.[50] This comparison further indicates that the small tracers couple to local fluctuations (which decrease with increasing ϕ) as well as matrix relaxations.[38]

Finally, we extract the relaxation time τ_r at $q\sigma_s \approx 0.07$ by fitting the DDM curves to a stretched exponential function and thereby extract a relaxation time τ_r. (The values that we obtain from this fitting protocol are in quantitative agreement with those determined by choosing τ_r satisfying $f(q,\tau=\tau_r) = 1/e$.) The characteristic relaxation time increases with ϕ at constant δ and decreases with δ at constant ϕ, consistent with expectations (Fig. 9 and S8). Although the range of (δ, ϕ) for which we are able to determine τ_r is very limited, our data for lower δ are consistent with the faster than exponential increase with ϕ, as predicted by Ref. 51.

4 Conclusions

We investigated the dynamics of tracer nanoparticles with tracer-matrix size ratios of $\delta = (0.34, 0.36, 0.45, 0.71)$ in a dense nanoparticle suspension using single-particle tracking (SPT) and differential dynamic microscopy (DDM). The tracer dynamics are strongly influenced by the size ratio δ and matrix ϕ, in qualitative agreement with previous studies of larger colloidal particles[34], despite

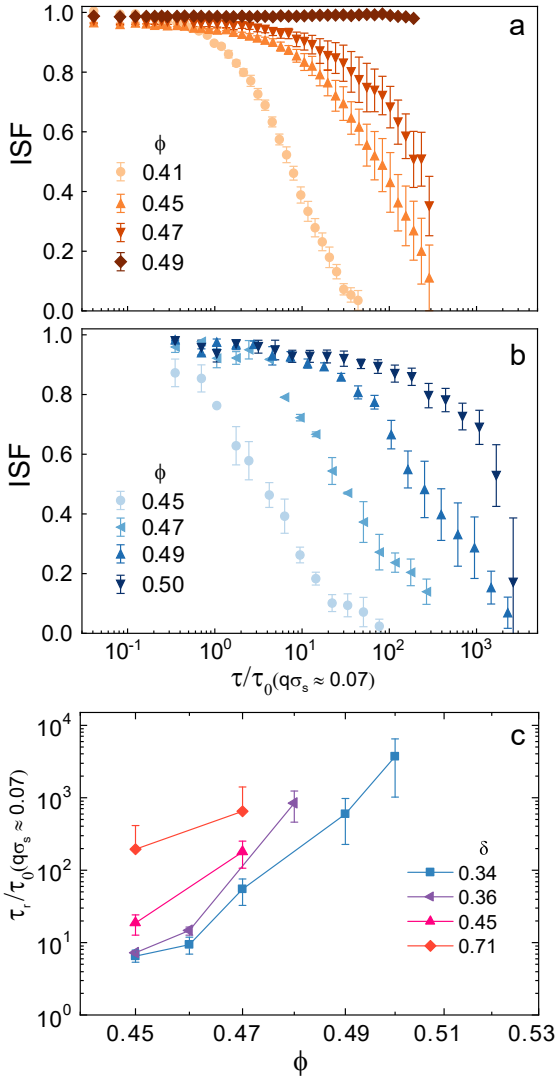

Fig. 9 (a, b) Intermediate scattering function $f(q,\tau)$ as a function of τ/τ_0 and ϕ at $q\sigma_s \approx 0.07$ for δ of (a) 0.71 and (b) 0.34. (c) Normalized tracer relaxation time τ_r/τ_0 at $q\sigma_s \approx 0.07$ as a function of ϕ for various δ. The error bars indicate the standard deviation of measurements of at least four samples.

the difference in the range and length scale of interparticle interactions, as well as our earlier computational studies[36,38]. For all δ, tracer dynamics determined from SPT slow and become increasingly subdiffusive as ϕ increases; for tracers with $\delta \geq 0.45$, the dynamics fully arrest at the highest accessible ϕ. Tracer displacements decrease on both short and long time scales as ϕ is increased, and this decrease is more pronounced for larger tracers ($\delta = 0.45, 0.71$) than for the smaller tracers ($\delta = 0.34, 0.36$). Measurements of collective dynamics using DDM reveal that small tracers ($\delta = 0.34, 0.36$) can exhibit anomalous logarithmic decays at length scales near $L \approx 6\sigma_{\text{matrix(i)}}$ for certain ϕ. The value of $\delta_c \approx 0.35$ is consistent with that determined in earlier studies.[34,36,37] The length scale of these dynamics ($L \approx 4-10\sigma_{\text{matrix(i)}}$), however, is somewhat larger in the nanoparticle experiments than in the earlier colloidal experiments of Ref. 34.We speculate that the longer length scale is due to the differences in the interparticle interactions, which are dominated by electrostatic repulsions in our nanoparticle system but were nearly-hard-sphere in the colloidal experiments of Ref. 34. Experiments to measure how electrostatic interactions affect the structure of the matrix (inaccessible in our system) as well as the frequency of interparticle contacts may provide insight into this increase in coupling length scale.

Together, our SPT and DDM results are consistent with the idea that the mechanism of nanoparticle transport in particulate matrices depends on the tracer-matrix size ratio. Specifically, larger particles appear to couple primarily to matrix relaxations, whereas small particles appear to couple both to matrix fluctuations and relaxations.[34,38] Intriguingly, electrostatic interactions do not appear to significantly affect the effective tracer size in this PS-PS system, whereas in our earlier study of silica tracers in a PS nanoparticle matrix[37] the localization followed the effective tracer size. Future studies in which the interactions between the tracer and matrix nanoparticles are systematically varied for matrix volume fractions spanning the supercooled to glass-forming regimes thus may provide additional insight into the role of interactions on the value of the critical size ratio as well as the coupling of tracer and matrix dynamics. Importantly, modifying the tracer-matrix interactions may alter the local structure of the matrix near the tracer.[68] Finally, the physical origin of the 4 – 10 particle length scale of the anomalous dynamics is unclear. It would be interesting to test, using superresolution methods[69] to resolve both matrix and tracer particles, whether this length scale is related to structure within the matrix, e.g. medium-range order,[70–73] or to a length scale characterizing matrix dynamics.[74–76]

Conflicts of interest

There are no conflicts to declare.

Acknowledgements

We thank Professors Alamgir Karim and Peter Vekilov (UH) for access to dynamic light scattering and Professor Ryan McGorty (University of San Diego) for training in the use of his DDM code. We acknowledge the support from the National Science Foundation (CBET-2004652) and the Welch Foundation (Grant E-1869-2024-0404). Representative movies for the four size ratios can be downloaded at: doi 10.17605/OSF.IO/6B7W4.

Notes and references

1 B. S. Schuster, J. S. Suk, G. F. Woodworth and J. Hanes, *Biomaterials*, 2013, **34**, 3439–3446.
2 H. ShamsiJazeyi, C. A. Miller, M. S. Wong, J. M. Tour and R. Verduzco, *Journal of Applied Polymer Science*, 2014, **131**,.
3 H. Zhang, A. Nikolov and D. Wasan, *Energy & Fuels*, 2014, **28**, 3002–3009.
4 S. Etemad, A. Kantzas and S. Bryant, *Fuel*, 2020, **276**, 118063.
5 J. Foroozesh and S. Kumar, *Journal of Molecular Liquids*, 2020, **316**, 113876.
6 R. Gharibshahi, M. Omidkhah, A. Jafari and Z. Fakhroueian, *Korean Journal of Chemical Engineering*, 2022, **39**, 562–575.

7 C. Song, H. Jang and J. Lee, *Colloids and Surfaces A: Physicochemical and Engineering Aspects*, 2023, **674**, 131910.

8 G. F. Paciotti, L. Myer, D. Weinreich, D. Goia, N. Pavel, R. E. McLaughlin and L. Tamarkin, *Drug Delivery*, 2004, **11**, 169–183.

9 G. F. Paciotti, D. G. Kingston and L. Tamarkin, *Drug Development Research*, 2006, **67**, 47–54.

10 S. K. Lai, Y.-Y. Wang, K. Hida, R. Cone and J. Hanes, *Proceedings of the National Academy of Sciences*, 2010, **107**, 598–603.

11 N. Ahmed, H. Fessi and A. Elaissari, *Drug Discovery Today*, 2012, **17**, 928–934.

12 A. K. Mehata, M. K. Viswanadh, P. Prasanna, M. Kumar and M. S. Muthu, in *Theranostic Applications of Upconversion Nanoparticle-Based Drug-Delivery Systems*, ed. C. V. Pardeshi, Springer International Publishing, Cham, 2023, pp. 239–268.

13 B. K. Kashyap, V. V. Singh, M. K. Solanki, A. Kumar, J. Ruokolainen and K. K. Kesari, *ACS Omega*, 2023, **8**, 14290–14320.

14 B. Ash, L. Schadler and R. Siegel, *Materials Letters*, 2002, **55**, 83–87.

15 I. Kohli and A. Mukhopadhyay, *Macromolecules*, 2012, **45**, 6143–6149.

16 R. Poling-Skutvik, R. Krishnamoorti and J. C. Conrad, *ACS Macro Letters*, 2015, **4**, 1169–1173.

17 L. Maldonado-Camargo, C. Yang and C. Rinaldi, *Nanoscale*, 2017, **9**, 12039–12050.

18 R. Chen, R. Poling-Skutvik, A. Nikoubashman, M. P. Howard, J. C. Conrad and J. C. Palmer, *Macromolecules*, 2018, **51**, 1865–1872.

19 R. Chen, R. Poling-Skutvik, M. P. Howard, A. Nikoubashman, S. A. Egorov, J. C. Conrad and J. C. Palmer, *Soft Matter*, 2019, **15**, 1260–1268.

20 R. Chen, S. B. Kotkar, R. Poling-Skutvik, M. P. Howard, A. Nikoubashman, J. C. Conrad and J. C. Palmer, *Journal of Rheology*, 2021, **65**, 745–755.

21 M. E. Mackay, T. T. Dao, A. Tuteja, D. L. Ho, B. V. Horn, H.-C. Kim and C. J. Hawker, *Nature Materials*, 2003, **2**, 762–766.

22 H. Guo, G. Bourret, M. K. Corbierre, S. Rucareanu, R. B. Lennox, K. Laaziri, L. Piche, M. Sutton, J. L. Harden and R. L. Leheny, *Phys. Rev. Lett.*, 2009, **102**, 075702.

23 S. Gam, J. S. Meth, S. G. Zane, C. Chi, B. A. Wood, M. E. Seitz, K. I. Winey, N. Clarke and R. J. Composto, *Macromolecules*, 2011, **44**, 3494–3501.

24 C. A. Grabowski and A. Mukhopadhyay, *Macromolecules*, 2014, **47**, 7238–7242.

25 P. J. Griffin, V. Bocharova, L. R. Middleton, R. J. Composto, N. Clarke, K. S. Schweizer and K. I. Winey, *ACS Macro Letters*, 2016, **5**, 1141–1145.

26 E. J. Bailey, P. J. Griffin, R. J. Composto and K. I. Winey, *Macromolecules*, 2019, **52**, 2181–2188.

27 E. J. Bailey and K. I. Winey, *Progress in Polymer Science*, 2020, **105**, 101242.

28 T. Moschakis, B. S. Murray and E. Dickinson, *Langmuir*, 2006, **22**, 4710–4719.

29 D. P. Keane, C. J. Constantine, M. D. Mellor and R. Poling-Skutvik, *AIChE Journal*, 2024, **70**, e18307.

30 S. Babu, J. C. Gimel and T. Nicolai, *The Journal of Physical Chemistry B*, 2008, **112**, 743–748.

31 S. Kaloun, R. Skouri, M. Skouri, J. P. Munch and F. Schosseler, *Phys. Rev. E*, 2005, **72**, 011403.

32 F. Schosseler, S. Kaloun, M. Skouri and J. P. Munch, *Phys. Rev. E*, 2006, **73**, 021401.

33 D. R. Strachan, G. C. Kalur and S. R. Raghavan, *Phys. Rev. E*, 2006, **73**, 041509.

34 T. Sentjabrskaja, E. Zaccarelli, C. De Michele, F. Sciortino, P. Tartaglia, T. Voigtmann, S. U. Egelhaaf and M. Laurati, *Nature communications*, 2016, **7**, 11133.

35 M. Laurati, T. Sentjabrskaja, J. Ruiz-Franco, S. U. Egelhaaf and E. Zaccarelli, *Phys. Chem. Chem. Phys.*, 2018, **20**, 18630–18638.

36 R. C. Roberts, R. Poling-Skutvik, J. C. Palmer and J. C. Conrad, *The Journal of Physical Chemistry Letters*, 2018, **9**, 3008–3013.

37 R. Poling-Skutvik, R. C. Roberts, A. H. Slim, S. Narayanan, R. Krishnamoorti, J. C. Palmer and J. C. Conrad, *The Journal of Physical Chemistry Letters*, 2019, **10**, 1784–1789.

38 R. Roberts, R. Poling-Skutvik, J. Conrad and J. Palmer, *The Journal of Chemical Physics*, 2019, **151**, 194501.

39 B. Mei and K. S. Schweizer, *The Journal of Chemical Physics*, 2021, **155**, 054505.

40 B. Mei, G. S. Sheridan, C. M. Evans and K. S. Schweizer, *Proceedings of the National Academy of Sciences*, 2022, **119**, e2210094119.

41 W. Kob, C. Donati, S. J. Plimpton, P. H. Poole and S. C. Glotzer, *Phys. Rev. Lett.*, 1997, **79**, 2827–2830.

42 R. Pastore, G. Pesce, A. Sasso and M. Pica Ciamarra, *The Journal of Physical Chemistry Letters*, 2017, **8**, 1562–1568.

43 J. Stevenson, J. Schmalian and P. Wolynes, *Nature Physics*, 2005, **2**,.

44 J. P. Garrahan and D. Chandler, *Phys. Rev. Lett.*, 2002, **89**, 035704.

45 C. Donati, J. F. Douglas, W. Kob, S. J. Plimpton, P. H. Poole and S. C. Glotzer, *Phys. Rev. Lett.*, 1998, **80**, 2338–2341.

46 G. Biroli and C. Cammarota, *Phys. Rev. X*, 2017, **7**, 011011.

47 L. Ortlieb, T. S. Ingebrigtsen, J. E. Hallett, F. Turci and C. P. Royall, *Nature Communications*, 2023, **14**, 2621.

48 Z. Zhang, P. J. Yunker, P. Habdas and A. G. Yodh, *Phys. Rev. Lett.*, 2011, **107**, 208303.

49 P. Pusey and W. van Megen, *Nature*, 1986, **320**, 340–342.

50 E. R. Weeks, J. C. Crocker, A. C. Levitt, A. Schofield and D. A. Weitz, *Science*, 2000, **287**, 627–631.

51 B. Mei and K. S. Schweizer, *Soft Matter*, 2021, **17**, 2624–2639.

52 B. Ju and T. Fan, *Powder Technology*, 2009, **192**, 195–202.

53 S. Ohta, E. Kikuchi, A. Ishijima, T. Azuma, I. Sakuma and T. Ito, *Scientific Reports*, 2020, **10**, 18220.

54 W. Kob and H. C. Andersen, *Phys. Rev. E*, 1995, **52**, 4134–4153.

55 J. C. Crocker and D. G. Grier, *Journal of Colloid and Interface Science*, 1996, **179**, 298–310.

56 R. Cerbino and V. Trappe, *Phys. Rev. Lett.*, 2008, **100**, 188102.

57 A. V. Bayles, T. M. Squires and M. E. Helgeson, *Rheologica Acta*, 2017, **56**, 863–869.

58 H. N. Verwei1, G. Lee, G. Leech, I. I. Petitjean, G. H. Koenderink, R. M. Robertson-Anderson and R. J. McGorty, *JoVE*, 2022, **184**, e63931.

59 F. Giavazzi, D. Brogioli, V. Trappe, T. Bellini and R. Cerbino, *Phys. Rev. E*, 2009, **80**, 031403.

60 M. S. Safari, R. Poling-Skutvik, P. G. Vekilov and J. C. Conrad, *npj Microgravity*, 2017, **3**, 21.

61 C.-C. Lin, E. Parrish and R. J. Composto, *Macromolecules*, 2016, **49**, 5755–5772.

62 M. Collins, F. Mohajerani, S. Ghosh, R. Guha, T.-H. Lee, P. J. Butler, A. Sen and D. Velegol, *ACS Nano*, 2019, **13**, 8946–8956.

63 H. Joung, C. Kim, J. Yu, S. Lee, K. Paeng and J. Yang, *Nano Letters*, 2022, **22**, 5487–5494.

64 F. Giavazzi, V. Trappe and R. Cerbino, *Journal of Physics: Condensed Matter*, 2020, **33**, 024002.

65 B. J. Berne and R. Pecora, *Dynamic Light Scattering: With Applications to Chemistry, Biology, and Physics*, Courier Corporation, 2000.

66 J. A. Barker and D. Henderson, *The Journal of Chemical Physics*, 1967, **47**, 2856–2861.

67 A. Fortini, M. Dijkstra and R. Tuinier, *Journal of Physics: Condensed Matter*, 2005, **17**, 7783.

68 B. Mei and K. S. Schweizer, *Macromolecules*, 2022, **55**, 9134–9151.

69 J. E. Hallett, F. Turci and C. P. Royall, *Nature Communications*, 2018, **9**, 3272.

70 T. Egami and C. W. Ryu, *Phys. Rev. E*, 2021, **104**, 064110.

71 C. W. Ryu and T. Egami, *Phys. Rev. E*, 2021, **104**, 064109.

72 T. Egami and C. W. Ryu, *Journal of Physics: Condensed Matter*, 2023, **35**, 174002.

73 T. Egami and C. W. Ryu, *AIP Advances*, 2023, **13**, 085308.

74 L. Berthier and R. L. Jack, *Phys. Rev. E*, 2007, **76**, 041509.

75 S. Karmakar, C. Dasgupta and S. Sastry, *Proceedings of the National Academy of Sciences*, 2009, **106**, 3675–3679.

76 R. Das, I. Tah and S. Karmakar, *The Journal of Chemical Physics*, 2018, **149**, 024501.

Selected movies are available online at doi: 10.17605/OSF.IO/6B7W4. All data are available upon reasonable request from the corresponding author (JCC).